

Two-magnon excitations observed by neutron scattering in the two-dimensional spin-5/2 Heisenberg antiferromagnet Rb_2MnF_4

T. Huberman, R. Coldea, R. A. Cowley

Oxford Physics, Clarendon Laboratory, Parks Road, Oxford OX1 3PU, UK

D. A. Tennant

*School of Physics and Astronomy, University of St Andrews,
North Haugh, St Andrews, FIFE KY16 9SS, Scotland, UK*

R. L. Leheny

Department of Physics and Astronomy, Johns Hopkins University, Baltimore, Maryland 21218, USA

R. J. Christianson

Department of Physics & DEAS, Harvard University, Cambridge, Massachusetts 02138, USA

C. D. Frost

Rutherford Appleton Laboratory, Chilton, Didcot, Oxon OX11 0QX, UK

(Dated: October 8, 2018)

The low-temperature magnetic excitations of the two-dimensional spin-5/2 square-lattice Heisenberg antiferromagnet Rb_2MnF_4 have been probed using pulsed inelastic neutron scattering. In addition to dominant sharp peaks identified with one-magnon excitations, a relatively weak continuum scattering is also observed at higher energies. This is attributed to neutron scattering by pairs of magnons and the observed intensities are consistent with predictions of spin wave theory.

PACS numbers: 75.40.Gb, 75.30.Ds, 75.10.Jm, 75.50.Ee

I. INTRODUCTION

Rb_2MnF_4 is a near-ideal two-dimensional spin-5/2 Heisenberg antiferromagnet on a square lattice (2DHASL) and has been extensively studied experimentally^{1,2,3,4} to test theoretical predictions for this canonical 2D quantum Hamiltonian. Neutron scattering experiments observe sharp one-magnon excitations at low temperatures which could be well described by linear spin wave theory.⁴ However, spin wave theory predicts that neutrons can also scatter from pairs of magnons leading to a broad scattering continuum at higher energies. Such processes are longitudinally polarized with respect to the ordered spin direction and correspond physically to the simultaneous creation of two magnons with opposite spin $S_z = \pm 1$ (total $\Delta S_z = 0$ process). The overall scattering weight of the two-magnon continuum relative to one-magnon processes is related to the relative strength of the zero-point longitudinal quantum fluctuations in the ground state, which reduce the amount of ordered spin moment by ΔS compared to the full spin value S . Very sensitive experiments are required to search for two-magnon continuum scattering since for spin-5/2 the two-magnon scattering intensity integrated over energy and wavevector is expected to be only of the order 6% of the integrated one-magnon intensity.

Another probe of two-magnon processes is light or Raman scattering and experiments on several 2DHAFSL systems have been made. Measurements in the $S=1$ system K_2NiF_4 ^{5,6} were found to be in excellent agree-

ment with calculations based on interacting spin wave theory. Similar experiments on the cuprates ($S=1/2$) have, however, shown a clear discrepancy between the observed lineshape and calculations based on spin wave theory for pure 2DHAFSL.⁷ The discrepancy is believed to arise from the presence of the four-spin cyclic exchange terms,^{8,9} which are also used to explain the observed spin wave dispersion along the antiferromagnetic zone boundary in La_2CuO_4 ref. 10.

Neutron scattering (unlike Raman scattering which has inherent momentum constraints) can in principle access the full wavevector and energy dependence of the two-magnon scattering. Raman and neutron scattering offer complementary information in that neutron intensities are related to two-operator correlation functions, whereas Raman is related to four-operator terms.

So far, two-magnon continuum scattering has been observed in the 3D material CoF_2 ^{11,12}, but little has been done to quantitatively measure the two-magnon scattering using neutrons in 2DHAFSL systems, the only other experiments we are aware of are on the spin-1/2 material $\text{Cu}(\text{DCOO})_2 \cdot 4\text{D}_2\text{O}$ (CFTD).¹³ The large quantum corrections in $S=1/2$ systems make it important to measure the two-magnon scattering in Rb_2MnF_4 with $S = 5/2$ where quantum fluctuations are expected to be smaller and to test the extent to which spin wave theory can describe the results.

The purpose of this paper is threefold. Firstly we wished to measure the spin waves with the MAPS spectrometer at ISIS to investigate whether high quality measurements of the dispersion relation could be made with

a neutron time-of-flight spectrometer as compared with earlier triple-axis measurements.⁴ Secondly we wished to study the spin wave energy along the antiferromagnetic zone boundary to search for evidence of four-spin interactions, second neighbour exchange interactions or quantum corrections to linear spin wave theory. Thirdly we wished to look for the two-magnon scattering continuum predicted by spin wave theory but lacking experimental evidence.

The rest of the paper is organized as follows. In Sec. II we review the spin wave theory predictions for one- and two-magnon scattering. Details of the experiment are given in Sec. III, followed in Sec. IV by results for the main dispersion relation with particular attention to wavevectors on the antiferromagnetic zone boundary. Sec. V reports on the observation of two-magnon scattering. The results are summarized in a final Sec VI.

II. DYNAMICAL CORRELATIONS

Rb_2MnF_4 crystallizes in the tetragonal K_2NiF_4 structure with space group $I4/mmm$ and lattice parameters $a = b = 4.215\text{\AA}$, $c = 13.77\text{\AA}$. The magnetic ions are Mn^{2+} with a spin-only moment of $S = 5/2$, arranged in a square lattice in the basal plane, with antiferromagnetic superexchange couplings between nearest neighbours mediated by intervening F^- ions. The inter-plane coupling is a factor of 10^{-4} of the intra-plane coupling¹⁴. This almost perfect two-dimensionality arises because MnF_2 magnetic layers have a large separation along the c -axis filled by two non-magnetic RbF sheets, and furthermore the magnetic couplings along c are frustrated because each Mn^{2+} ion is equidistant to four antiferromagnetically-coupled spins in the layers below and above, further weakening the effect of the inter-plane couplings.

Antiferromagnetic order with moments along the c -axis occurs below $T_N = 38.4$ K. Earlier studies² proposed that the observed ordering at finite temperature can be well accounted for by a small anisotropy $\delta_z = 0.0048(10)$ in the Hamiltonian, ultimately originating from dipolar interactions, i.e.

$$\hat{H} = J \sum_{\langle ii' \rangle} [S_i^x S_{i'}^x + S_i^y S_{i'}^y + (1 + \delta_z) S_i^z S_{i'}^z], \quad (1)$$

where $J = 0.6544(14)$ meV [ref. 4] is the exchange energy for nearest-neighbour spins on the square lattice and $\langle ii' \rangle$ indicates that each interacting spin pair is counted once in the summation. (x, y, z) are along the crystallographic (a, b, c) axes. For this Hamiltonian the magnon dispersion relation in linear spin wave theory is⁴

$$\omega_{\mathbf{Q}} = 4JS \left[(1 + \delta_z)^2 - \gamma_{\mathbf{Q}}^2 \right]^{\frac{1}{2}} \quad (2)$$

where $\gamma_{\mathbf{Q}} = \cos \pi(Q_k + Q_h) \cos \pi(-Q_k + Q_h)$ and (Q_h, Q_k, Q_l) are components of the crystal momentum

\mathbf{Q} given in rlu units of $(2\pi/a, 2\pi/b, 2\pi/c)$. Often a multiplicative factor, $Z_c = (1 + 0.157/2S)$, is included in the dispersion relation to account for corrections to lowest order spin wave theory. For $S = 5/2$, $Z_c = 1.0314$, and we neglect this correction as it can be readily incorporated into the exchange constant.

Neutron scattering measures the dynamical correlation functions given by

$$S^{\alpha\alpha}(\mathbf{Q}, \omega) = \frac{1}{2\pi\hbar N} \int_{-\infty}^{\infty} dt e^{-i\omega t} \sum_{ii'} e^{i\mathbf{Q} \cdot (\mathbf{r}_i - \mathbf{r}_{i'})} \langle S_{i'}^{\alpha}(0) S_i^{\alpha}(t) \rangle \quad (3)$$

where N is the total number of spins and the sum runs over all sites i and i' in the lattice. One-magnon events occur in the spin correlations *transverse* to the ordered spin direction z . In the non-interacting spin wave approximation the transverse correlations at $T = 0$ K are given by¹⁵

$$S^{xx}(\mathbf{Q}, \omega) = S^{yy}(\mathbf{Q}, \omega) = \frac{1}{2}(S - \Delta S)(u_{\mathbf{Q}} + v_{\mathbf{Q}})^2 \delta(\hbar\omega - \hbar\omega_{\mathbf{Q}}) \quad (4)$$

where $u_{\mathbf{Q}} = \cosh \theta$, $v_{\mathbf{Q}} = \sinh \theta$, $\tanh 2\theta = -\frac{\gamma_{\mathbf{Q}}}{(1 + \delta_z)}$. Here $\Delta S = S - \langle S^z \rangle$ is the spin reduction due to zero-point fluctuations calculated as $(1/N) \sum_{\mathbf{Q}} v_{\mathbf{Q}}^2$ where the sum extends over \mathbf{Q} 's in the full Brillouin zone. $\Delta S = 0.197$ for the isotropic Heisenberg model and 0.167 for the anisotropy δ_z appropriate for Rb_2MnF_4 .

The finite spin reduction allows for the presence of *longitudinal* fluctuations, which can be described in terms of two-magnon scattering events. In the non-interacting spin wave approximation the longitudinal correlations at $T = 0$ K are¹⁵

$$S^{zz}(\mathbf{Q}, \omega)_{\text{inelastic}} = \frac{1}{N} \sum_{\mathbf{Q}_1, \mathbf{Q}_2} f(\mathbf{Q}_1, \mathbf{Q}_2) \times \delta(\mathbf{Q} - \mathbf{Q}_1 + \mathbf{Q}_2) \delta(\hbar\omega - \hbar\omega_{\mathbf{Q}_1} - \hbar\omega_{\mathbf{Q}_2}) \quad (5)$$

where $f(\mathbf{Q}_1, \mathbf{Q}_2) = \frac{1}{2}(u_{\mathbf{Q}_1}v_{\mathbf{Q}_2} - u_{\mathbf{Q}_2}v_{\mathbf{Q}_1})^2$ is the structure factor for creating two magnons at wavevectors \mathbf{Q}_1 and \mathbf{Q}_2 . In the summation, one of the two magnons (say \mathbf{Q}_1) is restricted to the first Brillouin zone. The above equation gives the inelastic part of the longitudinal correlations, the elastic part is simply the Bragg peak contribution $(S - \Delta S)^2 \delta(\hbar\omega) \delta(\mathbf{Q} - \mathbf{Q}_{\text{AF}} - \boldsymbol{\tau})$, where $\mathbf{Q}_{\text{AF}} = (0.5, 0.5)$ is the antiferromagnetic ordering wavevector and $\boldsymbol{\tau}$ is a vector of the reciprocal lattice.

An understanding of how the scattering cross-section is distributed between the elastic, one and two-magnon channels can be obtained by comparing the integrated scattered intensities. The total intensity integrated over energy and averaged over the Brillouin zone is given by the well known sum rule $\int S(\mathbf{Q}, \omega) d\mathbf{Q} d\hbar\omega = S(S + 1)$. Similar expressions can be derived for the individual scattering components, by integrating over the expressions

for the elastic, one-magnon eq. (4) and two-magnon eq. (5) components. The results are summarised in Table I.

| component | integrated intensity |
|---|---|
| $S(\mathbf{Q}, \omega)$ | $S(S+1) = 8.75$ |
| $S^{zz}(\mathbf{Q}, \omega)_{\text{elastic}}$ | $(S - \Delta S)^2 = 5.443$ |
| $S^{xx}(\mathbf{Q}, \omega) + S^{yy}(\mathbf{Q}, \omega)$ | $(S - \Delta S)(2\Delta S + 1) = 3.112$ |
| $S^{zz}(\mathbf{Q}, \omega)_{\text{inelastic}}$ | $\Delta S(\Delta S + 1) = 0.195$ |

TABLE I: Total sum rules for the different components of the scattering, evaluated for $S = 5/2$ and $\Delta S = 0.167$.

The inelastic neutron scattering intensity from one and two-magnon excitations is proportional to

$$(2 - p_z)S^{xx}(\mathbf{Q}, \omega) + p_z S^{zz}(\mathbf{Q}, \omega)_{\text{inelastic}} \quad (6)$$

where $p_z = 1 - \hat{Q}_z^2$ is the polarization factor for longitudinal scattering, \hat{Q}_z is the directional cosine of the wavevector \mathbf{Q} with respect to the c -axis. The proportionality factor between eq. (6) and neutron scattering intensity includes the magnetic form factor squared $F(\mathbf{Q})^2$ of Mn^{2+} ions.

III. EXPERIMENTAL DETAILS

The magnetic scattering was measured from a 13.4g single crystal of Rb_2MnF_4 using the MAPS spectrometer at the ISIS pulsed neutron source in the UK. The sample was enclosed in an aluminium can containing helium exchange gas and measurements reported here were made at the base temperature of 9.5 K. MAPS is a direct geometry time-of-flight instrument, equipped with a 16 m^2 array of position sensitive detectors, divided into nearly 4×10^4 separate detector elements. This allows collection of the inelastic scattering intensity in a highly pixelated 3D volume in the 4D (Q_h, Q_k, Q_l, ω) space, from which one can extract the intensity plot in a certain plane or along a certain direction as illustrated in Fig. 1b) and c). We describe the data in terms of the two in-plane wavevectors (Q_h, Q_k) and energy $\hbar\omega$ as the magnetism is two-dimensional and the inter-layer component Q_l only enters the magnetic scattering through the magnetic form factor $F(\mathbf{Q})$ and the polarization factor p_z with respect to the ordered spin direction, see eq. (6).

An incident neutron energy of 24.92 meV was selected to map the inelastic scattering over the whole dynamic range of one- and two-magnon scattering processes which extended up to 13 meV. A Fermi chopper spinning at 300 Hz gave an energy resolution of 0.75 ± 0.01 meV (FWHM) on the elastic line. Measurements were made with the two-dimensional magnetic layers arranged perpendicular to the incident neutron beam (orientation 1, $\mathbf{c} \parallel \mathbf{k}_i$, \mathbf{a} horizontal) and tilted by an angle $\psi = 45^\circ$ with respect to the incident beam direction (orientation 2, $(\mathbf{c}, \hat{\mathbf{k}}_i) = \psi$) to collect complementary data with different longitudinal

polarization p_z at the same two-dimensional wavevector and energy (Q_h, Q_k, ω) . Typical counting times for one crystal orientations were 20 hours at an average proton current of $170 \mu\text{A}$. To increase statistics the data was folded along symmetry-equivalent axes as illustrated in Fig. 2, four-fold in the c -axis along \mathbf{k}_i setup, and two-fold in the rotated configuration. The low angle detector bank $2\theta < 30^\circ$ provided coverage over most of the first Brillouin zone.

IV. SPIN WAVE DISPERSION RELATION

The magnon dispersion relation was determined from fits to energy scans at constant wavevector (Q_h, Q_k) and typical data is shown in Fig. 3. The scattering is dominated by a sharp one-magnon excitation and solid lines show fits to eq. (4), where the delta function $\delta(\hbar\omega - \hbar\omega_Q)$ is replaced by a resolution broadened Gaussian peak. The extracted spin wave dispersion along symmetry directions in the Brillouin zone is shown in Fig. 4. Data at the lowest energies is limited because of the difficulty in resolving the one-magnon peak from the elastic incoherent scattering. The solid line shows a fit to the dispersion relation in eq. (2) with a fitted exchange $J = 0.648 \pm 0.003$ meV and fixed anisotropy $\delta_z = 0.0048$, in agreement with the previous estimates of $J = 0.6544 \pm 0.0014$ meV obtained from triple-axis neutron measurements⁴.

Linear spin wave theory, eq. (2), predicts no dispersion along the antiferromagnetic zone boundary (central panel in Fig. 4) therefore an observed dispersion along this direction can give information about failures of the linear spin wave approximation or extra interactions in the Hamiltonian beyond the nearest-neighbour exchange. In the spin-1/2 organic material CFTD¹⁶, the zone boundary energy was observed to decrease from (0.25, 0.25) to (0.5, 0) by $6 \pm 1\%$, and this agreed with computational work on the $S = 1/2$ 2DHAFL using the Ising-limit expansion that predicts a dispersion of 7%¹⁷. The zone-boundary dispersion was therefore attributed to quantum corrections to linear spin wave theory. A spin wave calculation extended to order $1/S^2$ predicts the same sign but a much smaller magnitude (2%) of this dispersion¹⁸ than the series results, suggesting that higher order corrections would need to be considered to obtain a fully satisfactory theory. In La_2CuO_4 the observed zone-boundary dispersion had the opposite sign, increasing from (0.25, 0.25) to (0.5, 0) by 13%¹⁰. This effect was attributed to higher-order spin exchange terms in the Hamiltonian. La_2CuO_4 is a Mott insulator and a more appropriate description of the electronic states is in terms of a Hubbard model at half-filling, characterized by a kinetic energy gain from hopping, t , and potential energy cost, U , for two electrons occupying the same site. At small t electrons are localized, and perturbative expansion in t/U gives an effective Hamiltonian for the spin degrees of freedom. The first term in this expansion is the nearest-neighbour Heisenberg exchange, and the dominant next order term

FIG. 1: (Color online) (a) One-magnon dispersion surface as a function of two-dimensional wavevector (Q_h, Q_k) and energy ω (color shading is intensity in neutron scattering). Dashed lines in the basal plane and at maximum energy $\hbar\omega = 4JS$ mark the antiferromagnetic zone boundaries. The basal plane also shows constant-energy contours (solid lines). (b) Constant energy maps of the magnetic scattering at $\hbar\omega = 1, 3.5$ and 6 meV obtained by taking slices from the 3D (Q_h, Q_k, ω) neutron data. (c) Energy scan at constant wavevector $(-0.5, 0)$ along the direction shown by the vertical rectangular column in (b) (cross-section of column $\Delta Q_h \times \Delta Q_k$ indicates the wavevector region over which intensity points were averaged).

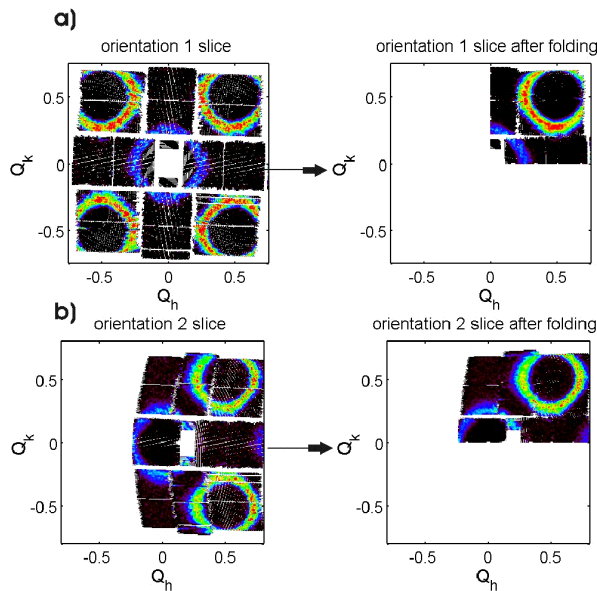
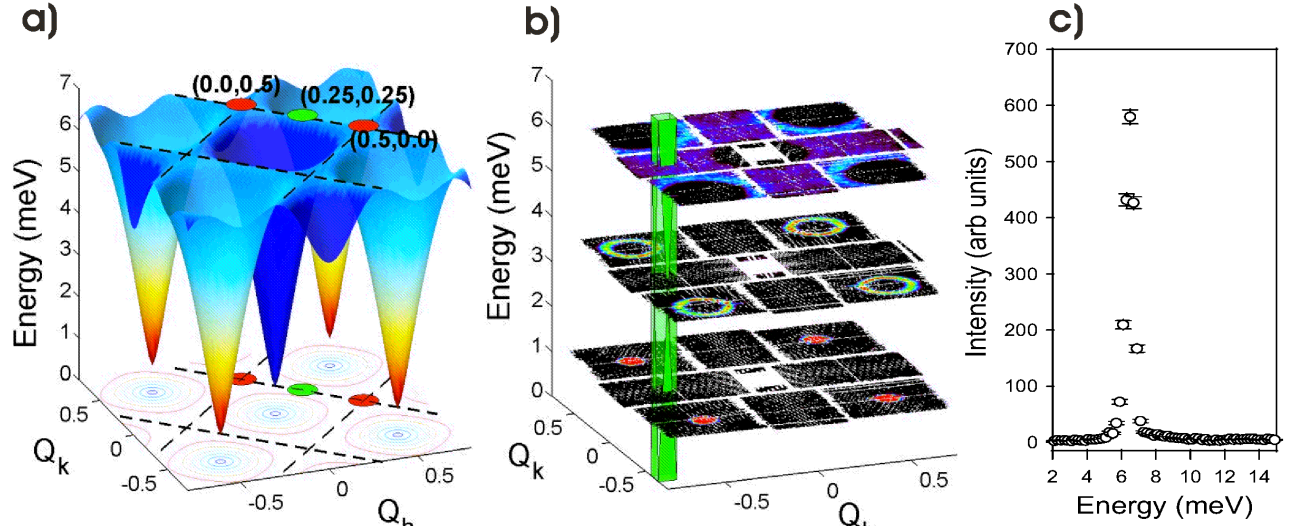


FIG. 2: (Color online) Folding of data along symmetry-equivalent directions: (a) four-fold symmetry in the $c \parallel k$ setup (b) two-fold symmetry in the rotated configuration. Data corresponds to intensity at an energy 5.5 ± 0.5 meV.

is a cyclic exchange coupling 4 spins at the corners of each square plaquette. Such a ring exchange term corresponding to $U/t \sim 6$ was used to describe the high-energy

magnon dispersion,¹⁰ Raman scattering⁸ and infrared absorption experiments¹⁹ in La_2CuO_4 .

The spin wave energies along the antiferromagnetic zone-boundary contour in Rb_2MnF_4 are shown in a blown-out scale in Fig. 5. The dispersion along the $Q_h + Q_k = 0.5$ direction is very small, of order $1 \pm 0.5\%$ between $(0.5, 0)$ and $(0.25, 0.25)$. In extracting peak positions we carefully considered the effects of wavevector averaging over a box of finite size $\Delta Q_h \times \Delta Q_k$ around the nominal (Q_h, Q_k) values. Since the dispersion surface has a maximum on the zone boundary, the effect of a finite wavevector averaging is to produce an apparently lower peak energy. The effect is more pronounced around the $(0.25, 0.25)$ point since there the dispersion surface has only a one-dimensional maximum, whereas the corner point $(0.5, 0)$ is a local maximum along two directions in the plane, see Fig. 1a). This effect is illustrated in Fig. 6 by taking cuts of different sizes $\Delta Q_h \times \Delta Q_k$ over a simulated data set for the one-magnon scattering cross-section, eq. (4). A wavevector box of size 0.04×0.04 was chosen as a balance between a minimal apparent peak shift ($< 0.1\%$) and sufficient data pixels in the box for sufficient statistics to allow quantitative analysis and the final results are shown in Fig. 5. Data collected under two sample orientations show a small dispersion with the higher energy at $(0.25, 0.25)$. The magnitude of the dispersion is small, $1 \pm 0.5\%$ of the zone boundary energy, a value close to the limit of the experimental accuracy, which may explain why the two data sets are not exactly overlapping.

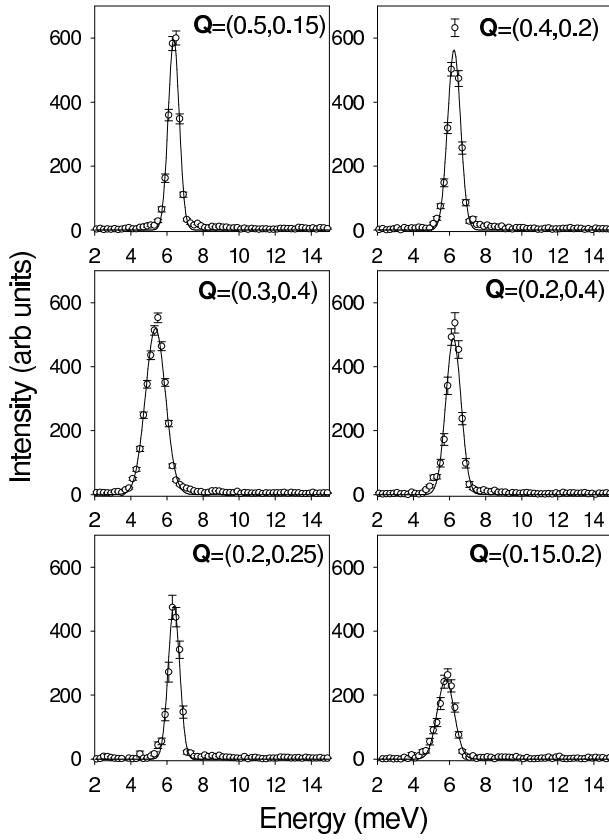


FIG. 3: Energy scans at constant (Q_h, Q_k) wavevector. Solid lines are fits to Gaussian peaks.

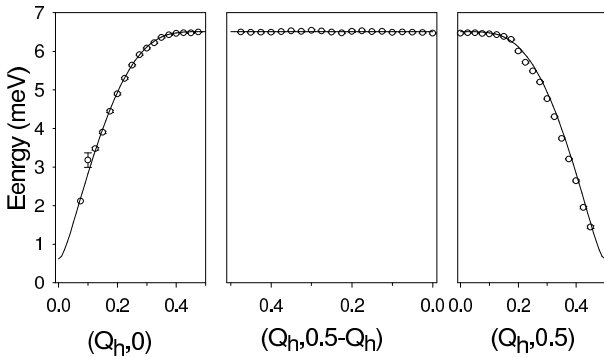


FIG. 4: Dispersion relation along symmetry directions in the Brillouin zone (bold lines in Fig. 7 b)). Solid line shows a fit to eq. (2) with $J = 0.648$ meV.

We note that quantum corrections to linear spin wave theory to order $1/S^2$ would predict a dispersion of the same sign but nearly an order of magnitude smaller, 0.005 meV¹⁸. Earlier triple-axis measurements also observed a dispersion similar to the one in the present experiments and Cowley *et al.*⁴ proposed that the origin was a next-

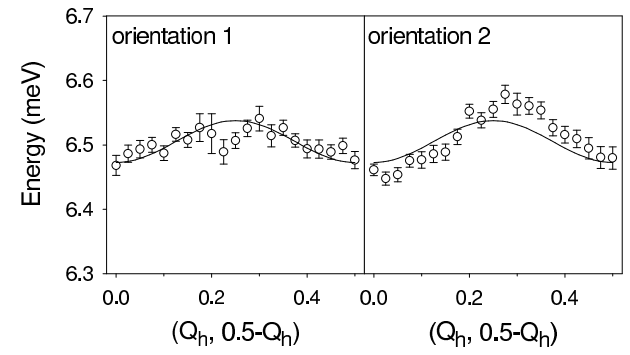


FIG. 5: Magnon energy for wavevectors along the antiferromagnetic zone boundary obtained using narrow (0.04×0.04) cuts from data collected under two different experimental set-ups. Solid line is a fit to the spin wave dispersion relation including next-nearest neighbour coupling, eq. (7).

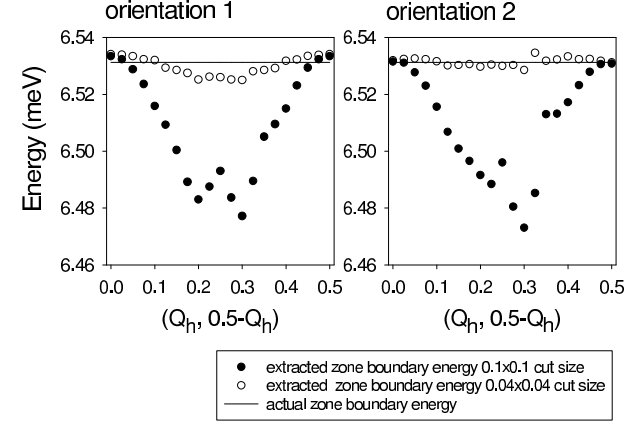


FIG. 6: Energy of one-magnon peak extracted from cuts through a simulated data set for eqs. (2,4). Using a large wavevector averaging range $\Delta Q_h \times \Delta Q_k = 0.1 \times 0.1$ around the nominal (Q_h, Q_k) position introduces an apparent dispersion of 0.9% (filled circles), whereas the smaller cut size 0.04×0.04 (open symbols) reduces this to less than 0.1%.

nearest neighbour antiferromagnetic exchange J' along the square diagonals. The dispersion relation in this case becomes

$$\hbar\omega_Q = 4JS \left[\left(1 + \delta_z + \frac{J'}{2J} \gamma'_Q \right)^2 - \gamma_Q^2 \right]^{1/2}, \quad (7)$$

where $\gamma_Q = \cos \pi(Q_k + Q_h) \cos \pi(-Q_k + Q_h)$, $\gamma'_Q = \cos[2\pi(Q_h + Q_k)] + \cos[2\pi(-Q_h + Q_k)] - 2$. We have fitted this expression to the dispersion along the zone boundary in Fig. 5 and the results are $J = 0.657 \pm 0.002$ meV, $J' = 0.006 \pm 0.003$ meV, compared to $J = 0.673 \pm 0.028$ meV, $J' = 0.012 \pm 0.002$ meV obtained previously⁴. The difference in J arises because the frequencies at the zone boundary are lower in our measurements due possibly to small errors in the absolute energy calibration in one of the two experiments.

In short the present experiments observe a definite change in energy along the antiferromagnetic zone boundary. The effect is small and the data barely produces a reliable estimate of the effect. Nevertheless, our results do suggest that its most probable origin is from the next nearest neighbour exchange constants. We shall however neglect this small effect for most of the remainder of this paper.

V. TWO-MAGNON CONTINUUM SCATTERING

To estimate the two-magnon scattering intensity predicted by spin wave theory we evaluated eq. (5) numerically by summation over a grid of finely spaced \mathbf{Q}_1 points over one Brillouin zone, setting $\mathbf{Q}_2 = \mathbf{Q} - \mathbf{Q}_1$ and replacing the delta function in energy with an area-normalized narrow Gaussian. Fig. 7a) shows an overview plot of the calculated two-magnon cross-section as a function of energy and wavevector along symmetry directions the Brillouin zone. Two-magnon scattering occurs in the form of a continuum at higher energies above the one-magnon dispersion relation. The small energy separation $E_{\text{gap}}(\mathbf{Q})$ between one- and two-magnon excitations is a consequence of the small uniaxial anisotropy δ_z in the Hamiltonian eq. (1), which opens a gap in the one-magnon spectrum at the zone centre $\hbar\omega_0 = 4JS\sqrt{\delta_z(2+\delta_z)}$, with two-magnon scattering starting at the higher energy of $2 \times \hbar\omega_0$. Generally the two-magnon intensity is strongest for low energies and wavevectors near the antiferromagnetic zone centre, but here is also where the one-magnon structure factor is largest. The clearest way to separate a scattering signal from one- and two-magnon processes is at energies above the one-magnon zone boundary, and Fig. 7b) shows a plot of the calculated two-magnon intensity distribution in the Brillouin zone at an energy 8.75 ± 1.25 meV, above the one-magnon cut-off.

Calculated lineshapes at representative points in the Brillouin zone are shown in Fig. 8. One noticeable feature is the appearance of strong singular peaks, which become more prominent upon increasing the numerical accuracy in evaluating eq. (5). The singularities are a result of divergencies in the two-magnon density of states obtained by putting $f = 1$ in eq. (5), i.e.

$$\begin{aligned} D(\mathbf{Q}, \omega) &= \frac{1}{N} \sum_{\mathbf{Q}_1, \mathbf{Q}_2} \delta(\mathbf{Q} - \mathbf{Q}_1 + \mathbf{Q}_2) \delta(\hbar\omega - \hbar\omega_{\mathbf{Q}_1} - \hbar\omega_{\mathbf{Q}_2}) \\ &= \frac{1}{N} \sum_{\mathbf{Q}_1} \delta(\hbar\omega - \hbar\omega_{\mathbf{Q}_1} - \hbar\omega_{\mathbf{Q} - \mathbf{Q}_1}) \end{aligned} \quad (8)$$

Plots of $D(\mathbf{Q}, \omega)$ are shown by dotted lines in Fig. 8. The singularities at the high energy boundary present in $D(\mathbf{Q}, \omega)$ do not show up in $S^{zz}(\mathbf{Q}, \omega)_{\text{inelastic}}$. This is because the structure factor of those processes in neutron scattering cancels as both magnons are on the antiferromagnetic zone boundary contour where $v_{\mathbf{Q}_1} = v_{\mathbf{Q}_2} = 0$.

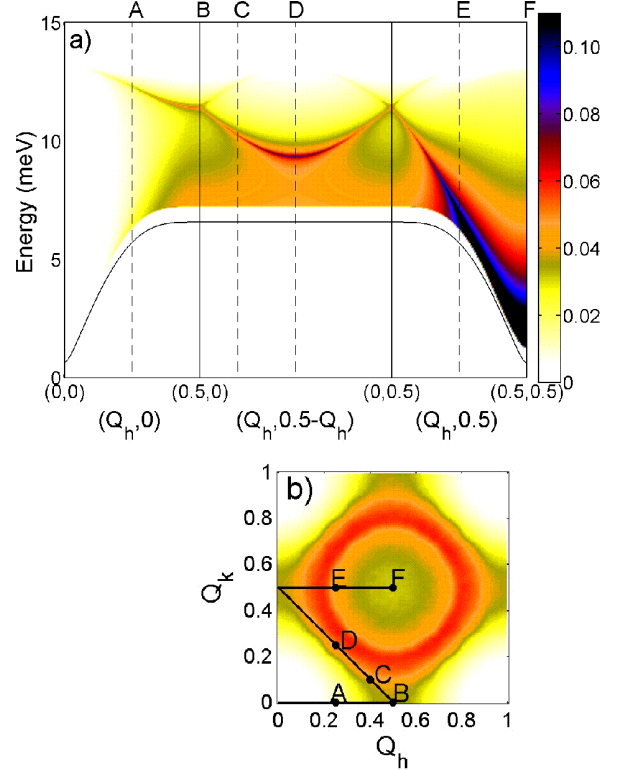


FIG. 7: (Color online) (a) Two-magnon scattering intensity $S^{zz}(\mathbf{Q}, \omega)_{\text{inelastic}}$ as a function of energy and wavevector along symmetry directions in the Brillouin zone (thick solid curve in (b)). Colour represents intensity. The solid line shows the one-magnon dispersion relation $\hbar\omega_{\mathbf{Q}}$ from eq.(2). (b) Two-magnon intensity as a function of wavevector at constant energy $\hbar\omega = 8.75 \pm 1.25$ meV. Lineshapes at positions labelled A-F are shown in Fig. 8.

It is interesting to consider whether any of the singularities are a true feature of the two-magnon neutron scattering or whether they are a consequence of using non-interacting spin wave theory. Canali and Wallin²⁰ have included first order spin wave interactions in calculating $S^{zz}(\mathbf{Q}, \omega)$ and their results show that the singularity peaks remain. However, any treatment of interactions within spin wave theory is perturbative and so it is possible higher order interactions may be still be important when considering the singularities. Experimentally, resolution effects would make the singularities very difficult to observe as shown in Fig. 8 where the two-magnon lineshapes are convoluted with the resolution in our experiment and the results (dashed lines) show that any singularity would probably not be visible in our measurements.

To test for the presence of two-magnon scattering in the data, we extracted energy cuts at fixed wavevectors (Q_h, Q_k) . Because of the inherently weak intensity of the two-magnon cross-section we chose a wavevector averaging range 0.1×0.1 to have enough data pixels for

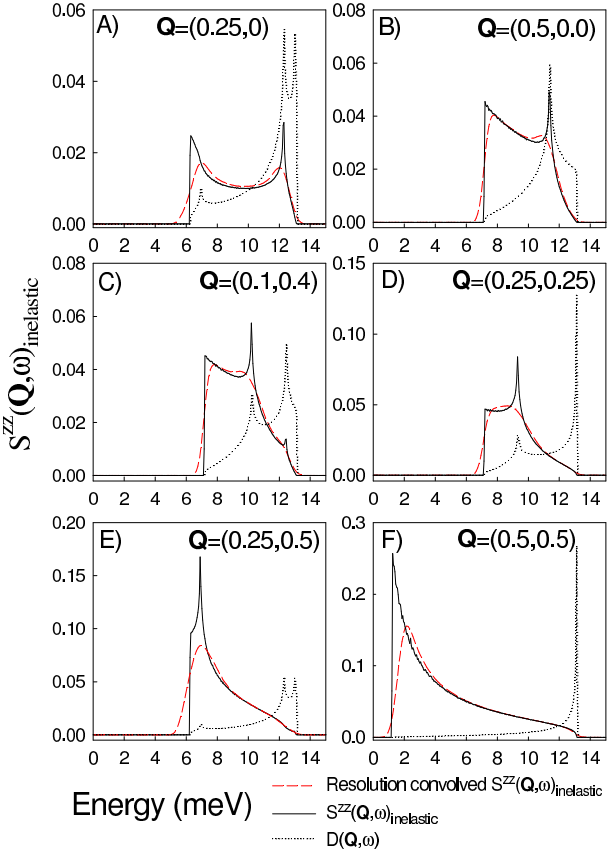


FIG. 8: Calculated two-magnon scattering lineshapes at fixed wavevectors, indicated by labels A-F in Fig. 7. Solid line is $S^{zz}(Q, \omega)_{inelastic}$ and dashed lines show the effects of the instrumental resolution. Dotted lines show the two-magnon density of states, $D(Q, \omega)$ eq. (8), divided by a factor of 10.

quantitative analysis. A typical scan near the antiferromagnetic zone boundary at $(0.5, 0.15)$ is shown in Fig. 9a). The inelastic scattering is dominated by a sharp, one-magnon peak centred at 6.40 ± 0.02 meV, and additional much weaker scattering is observed in the form of a high energy continuum tail extending to at least 9 meV [see Fig. 9d)], much higher than the one-magnon zone boundary energy.

Our approach is to fit the data to a lineshape containing both one and two-magnon components, with their relative intensity fixed by theory, eqs. (4), (5) and (6). The effects of resolution broadening are also included as discussed below. The effects of the finite cut size were included by averaging the predicted intensity over the finite wavevector size $\Delta Q_h \times \Delta Q_k$ of the cut. The resulting profile was then convolved with the energy resolution of the spectrometer. This was determined from the observed lineshape of the quasi-elastic peak in Fig. 9b). This showed a slightly asymmetric tail at lower energies (due to the asymmetric neutron pulse shape) and the whole profile could be well parameterized by a sum of two Gaussian peaks, one off-centred on the low-energy side,

see Fig. 9c). Such a weakly-asymmetric lineshape also provided a good description of the observed one-magnon peak lineshape as shown in Fig. 9d). The relative positions, intensities and widths of those two Gaussians are fixed while the fitted parameters are the overall width of the one-magnon peak (to parameterize the variation of the energy resolution with energy transfer) and an overall scale factor. Fig. 9e) shows that the whole observed scattering lineshape including the high-energy tail can be well described when the two-magnon cross-section is included.

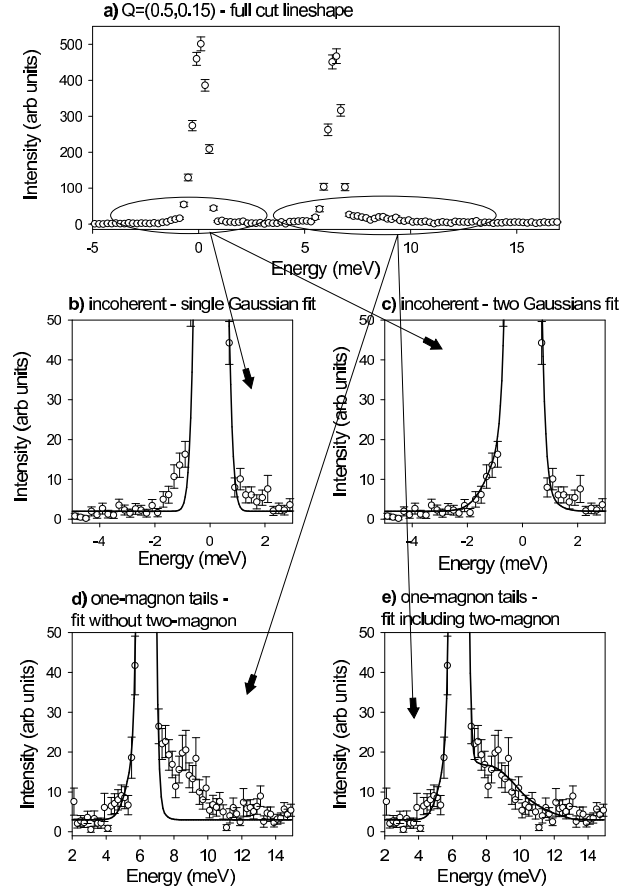


FIG. 9: Stages of the fitting procedure. a) Energy scan at $(0.5, 0.15)$. b)-c) Low-energy asymmetric lineshape of the incoherent scattering is well parameterized by a two Gaussian lineshape. d) Fitting the same resolution profile to the one-magnon peak centred at 6.40 meV, the extra scattering on the high-energy tail can not be accounted for by resolution effects. e) Fits to the combined one- and two-magnon scattering eq. (6) including resolution effects.

Fig. 10 shows the overall comparison between the observed intensity in the high-energy tails and that expected from two-magnon scattering. The plot corresponds to intensity averaged over the energy range 7.5 to 10 meV, much higher than that of the one-magnon zone boundary, where only two-magnon processes are expected to contribute. There is good overall agreement

between data and calculations, which include the longitudinal polarization factor p_z expected for two-magnon processes eq (6).

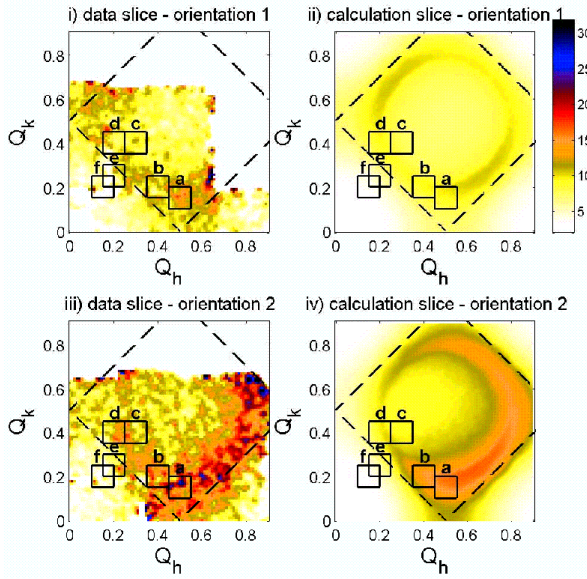


FIG. 10: (Color online) Comparison between data and predicted two-magnon scattering at an energy $\hbar\omega = 8.75 \pm 1.25$ meV, much higher than the one-magnon zone boundary energy. i) and iii) show data in two different experimental configurations and ii) and iv) show the simulated two-magnon scattering intensity including the polarization factor, magnetic form factor, an overall scale factor and a flat background to compare with data. Boxes labelled a)-f) show location of energy scans plotted in Fig. 11. The dashed square box is the antiferromagnetic zone boundary.

A number of representative energy scans extracted from the data near the antiferromagnetic zone boundary where the two-magnon contribution can most easily be singled out are shown in Fig. 11. Solid lines show the results of the fitting procedure described above to the combined one-and two-magnon scattering lineshapes eq. (6) and good agreement is observed throughout. In those fits the overall scale factor was allowed to vary for each scan, however very similar fits are obtained if this scale factor is fixed to a common average value for all scans and for clarity we only show the two-magnon component determined in this way (dashed lines), practically indistinguishable from the results of the free fits. As an independent consistency check we have converted the neutron intensities into absolute units of barn meV⁻¹ sr⁻¹ per spin normalizing by the sample mass and by intensities measured with a vanadium standard; the calculated two-magnon neutron scattering intensities in absolute units are very close (within 10%) to the results of the fits, this

agreement giving further support to the identification of the continuum intensities with two-magnon scattering.

The scans shown in Fig. 11 include points where the intensity from two-magnon scattering is predicted to be low, as well points where it is predicted to be high, this modulation of intensity being mainly due to the polarization factor p_z in eq. (6). For example scans in Fig. 11e)-f) have rather weak high-energy tails and cannot be taken in isolation to provide evidence of two-magnon scattering, but are significant when taken in the context of all the scans shown. The scans in Fig. 11a')-b') show the strongest high-energy signal, since they correspond to the largest longitudinal polarization factor appropriate for two-magnon scattering (and *lowest* polarization factor for transverse one-magnon scattering). Another illustration of the polarization effect is provided by comparing the data in Figs. 11b') and d') collected at equivalent positions in the Brillouin zone: using the same two-magnon intensity in both scans without adjusting for the change in polarization factor results in a large disagreement (dotted line in Fig. 11b') with the observed continuum scattering intensity. From this analysis we conclude that the observed continuum scattering at high energies is consistent both in magnitude and polarization with scattering expected from two-magnon processes, neglecting any interactions between the magnons.

VI. CONCLUSIONS

We have conducted a detailed investigation of the low temperature dynamical properties of the square-lattice spin-5/2 Heisenberg antiferromagnet Rb₂MnF₄. The spin wave dispersion was measured and a small variation in energy along the antiferromagnetic zone boundary was found. The energy change along the zone boundary was too large to be explained by quantum corrections to linear spin wave theory, and could be the result of weak next-nearest neighbour exchange interactions ($J'/J = 1 \pm 0.5\%$). Furthermore, a low intensity signal was observed around the high energy tail of the one-magnon peaks. The lineshape and intensity variation of this signal provides good evidence that it is the result of scattering by pairs of non-interacting spin waves (two-magnon scattering). We conclude that although spin wave interactions are important in describing the shape of the two-magnon Raman scattering, they are much less important for two-magnon neutron scattering.

This research was supported by UK EPSRC (TH, RC, RAC, DAT) and by US NSF through grant number DMR-0134377 (RLL). We are also grateful to the staff at ISIS for their help and support and to Bella Lake and Robert Birgeneau for useful discussions.

¹ R. J. Birgeneau, H. J. Guggenheim, and G. Shirane, Phys. Rev. B **8**, 304 (1973).

² R. J. Birgeneau, H. J. Guggenheim, and G. Shirane, Phys.

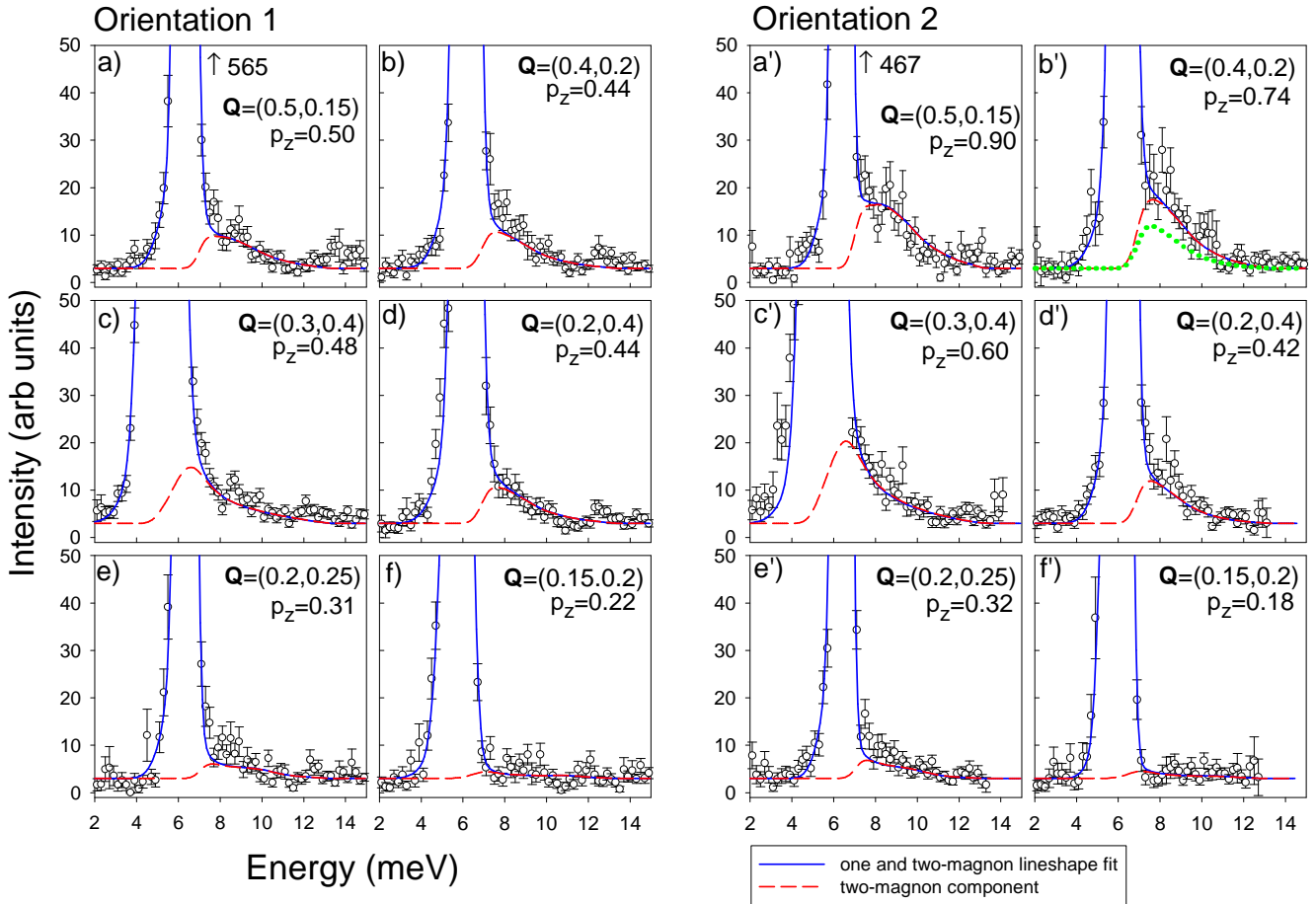


FIG. 11: (Color online) Energy scans analysed with a combined one and two-magnon cross-section eq. (6) (solid lines). Dashed lines shows the two-magnon component, with a common overall scale factor for all scans, as used in the simulation in Fig. 10. Scan labels a-f) (with ' for data in orientation 2) refer to locations in the Brillouin zone indicated in Fig. 10. p_z is the longitudinal polarization factor in the middle of the two-magnon continuum region at 8.75 meV. Dotted line in b') illustrates the type of disagreement obtained if one uses the two-magnon intensity observed at the equivalent position d') without adjusting for the change in polarization factor.

Rev. B **1**, 2211 (1970).

³ R. L. Leheny, R. J. Christianson, R. J. Birgeneau, and R. W. Erwin, Phys. Rev. Lett. **82**, 418 (1999).

⁴ R. A. Cowley, G. Shirane, R. J. Birgeneau, and H. G. Guggenheim, Phys. Rev. B **15**, 4292 (1977).

⁵ P. A. Fleury and H. J. Guggenheim, Phys. Rev. Lett. **24**, 1346 (1970).

⁶ S. R. Chinn, H. J. Zeiger, and J. R. O'connor, Phys. Rev. B **3**, 1709 (1971).

⁷ K. B. Lyons, P. E. Sulewski, P. A. Fleury, H. L. Carter, A. S. Cooper, G. P. Espinosa, Z. Fisk, and S.-W. Cheong, Phys. Rev. B **39**, R9693 (1989).

⁸ S. Sugai, M. Sato, T. Kobayashi, J. Akimitsu, T. Ito, H. Takagi, S. Uchida, S. Hosoya, T. Kajitani, and T. Fukuda, Phys. Rev. B **42**, R1045 (1990).

⁹ M. Roger and J. M. Delrieu, Phys. Rev. B **39**, 2299 (1989).

¹⁰ R. Coldea, S. M. Hayden, G. Aeppli, T. G. Perring, C. D. Frost, T. E. Mason, S.-W. Cheong, and Z. Fisk, Phys. Rev. Lett. **86**, 5377 (2001).

¹¹ R. A. Cowley, W. J. L. Buyers, P. Martel, and R. W. H. Stevenson, Phys. Rev. Lett. **23**, 86 (1969).

¹² T. M. Holden, E. C. Svensson, W. J. L. Buyers, R. A. Cowley, and R. W. H. Stevenson, Journal of Appl. Phys. **41**, 896 (1970).

¹³ N. B. Christensen, H. M. Rønnow, D. F. McMorrow, H. Harrison, G. Aeppli, T. G. Perring, R. Coldea, L. P. Regnault, and M. Enderle, to be published.

¹⁴ H. W. de Wijn, L. R. Walker, and R. E. Walstedt, Phys. Rev. B **8**, 285 (1973).

¹⁵ I. U. Heilmann, J. K. Kjems, Y. Endoh, G. F. Reiter, G. Shirane, and R. J. Birgeneau, Phys. Rev. B **24**, 3939 (1981).

¹⁶ H. M. Rønnow, D. F. McMorrow, R. Coldea, A. Harrison, I. D. Youngson, T. G. Perring, G. Aeppli, O. Syljuåsen, K. Lefmann, and C. Rischel, Phys. Rev. Lett. **87**, 37202 (2001).

¹⁷ R. R. P. Singh and M. P. Gelfand, Phys. Rev. B **52**, R15695 (1995).

¹⁸ C. M. Canali, S. M. Girvin, and M. Wallin, Phys. Rev. B **45**, R10131 (1992).

¹⁹ J. Lorenzana, J. Eroles, and S. Sorella, Phys. Rev. Lett. **83**, 5122 (1999).

²⁰ C. M. Canali and M. Wallin, Phys. Rev. B **48**, 3264 (1993).